COMMUNICATIONS PHYSICS

ARTICLE

https://doi.org/10.1038/s42005-019-0162-4 OPEN

Spectroscopy of the superconducting proximity effect in nanowires using integrated quantum dots

Christian Jünger[1], Andreas Baumgartner[1,2], Raphaëlle Delagrange[1], Denis Chevallier[1], Sebastian Lehmann[3], Malin Nilsson[3], Kimberly A. Dick[3,4], Claes Thelander[3] & Christian Schönenberger[1,2]

The superconducting proximity effect has recently attracted a renewed interest as the basis of topologically nontrivial states in materials with a large spin–orbit interaction, with protected boundary states useful for quantum information technologies. However, spectroscopy of these states is challenging because of the limited control of conventional tunnel barriers. Here we report electronic spectroscopy measurements of the proximity gap in a semiconducting indium arsenide nanowire segment coupled to a superconductor, using quantum dots formed deterministically during the crystal growth. We extract characteristic parameters describing the proximity gap, which is suppressed for lower electron densities and fully developed for larger ones. This gate-tunable transition of the proximity effect can be understood as a transition from the long to the short junction regime of subgap bound states in the NW segment. Our device architecture opens up the way to systematic, quantitative spectroscopy studies of subgap states, such as Majorana-bound states.

[1] Department of Physics, University of Basel, Klingelbergstrasse 82, CH-4056 Basel, Switzerland. [2] Swiss Nanoscience Institute, University of Basel, Klingelbergstrasse 82, CH-4056 Basel, Switzerland. [3] Division of Solid State Physics and NanoLund, Lund University, S-221 00 Lund, Sweden. [4] Center for Analysis and Synthesis, Lund University, S-221 00 Lund, Sweden. Correspondence and requests for materials should be addressed to C.J. (email: christian.juenger@unibas.ch) or to A.B. (email: andreas.baumgartner@unibas.ch)

Coupling a superconductor (SC) to a metal or a semiconductor results in the so-called superconducting proximity effect in the normal material[1]. If the proximitized material is a low-dimensional semiconductor, this phenomenon can, for example, be used as a source of spin-entangled electrons[2,3] or superconducting magnetometers[4]. By combining an *s*-wave SC with a one-dimensional semiconducting nanowire (NW) with large spin–orbit interaction, one can artificially create a proximity region with superconductivity of *p*-wave character. This can give rise to exotic quantum states at the ends of the SC, such as Majorana-bound states[5–8], potentially useful as building blocks for topological quantum information processing[9,10]. However, a systematic characterization of superconducting subgap states and the proximity region in NWs remains challenging. Several theoretical proposals suggest to use a quantum dot (QD) as a spectrometer to investigate Majorana-bound state lifetimes[11,12], spin texture[13], or parity[14]. A first experiment was reported recently in which the QD was defined by electrical gating[7]. However, systematic and deterministic spectroscopy requires a spatially well defined, weakly coupled QD with sharp tunnel barriers across the complete NW, which does not hybridize with the bound states or the SC under investigation. In contrast to earlier spectroscopy experiments in NWs[15,16], we use integrated QDs for the tunnel spectroscopy, which separates the spectrometer from the investigated region in a predictable way. To probe the evolution of the proximity effect in a NW segment close to the superconducting contact, we use an in-situ grown axial QD in an InAs NW, which homogeneously covers the complete diameter of the NW, in contrast to the standard gate-defined QDs. Compared with previous experiments investigating the spatial distribution and length scales of the superconducting proximity effect in metals[17,18], the semiconducting NWs also allow us to control the carrier density and all related parameters, such as the Fermi velocity, in the system. We demonstrate two types of tunnel spectroscopy distinguished by the transport mechanism through the integrated QD, both probing the NW density of states (DOS): the cotunneling regime, where the QD can be seen as a single tunnel barrier, and the sequential tunneling regime, where the QD acts as an energy filter with Coulomb blockade (CB) resonances. The complementary measurements allow us to draw a clear picture of how the proximity gap forms in a NW segment, for which we present an intuitive explanation supported by numerical simulations.

Results

Device and characterization. The QD is defined by two potential barriers that form when the NW crystal structure is changed from zincblende (ZB) to wurtzite (WZ), which can be achieved with atomic precision by controlling the growth parameters[19,20]. These QDs are electrically and spatially well defined, which allows us to probe the induced gap in the NW segment at a precise distance from the QD and with predictable coupling parameters. Similar in-situ grown barriers have been used previously to investigate double QD physics[21,22].

We use an InAs NW with an in-situ-grown axial QD formed by controlling its crystal phase structure in the growth direction[20]: two thin segments (30 nm) of WZ phase are grown in the otherwise ZB NW. These segments act as atomically precise hard-wall tunnel barriers for electrons, because the ZB and WZ band structure align with a conduction band offset of ~100 meV[23,24]. Consequently, a QD is formed in the ZB section (20 nm) between the two barriers[23]. A false color scanning electron micrograph of the device discussed here is shown in Fig. 1a, together with a transmission electron micrograph of the atomically precise interface in a representative NW, shown in the inset. The superconducting electrode consists of titanium/aluminum (Ti/Al) and the normal contact of titanium/gold (Ti/Au), fabricated by electron beam lithography. The differential conductance $G = dI/dV_{SD}$ as a function of the backgate voltage V_{BG} in the normal state (in an external magnetic field of $B =$ 50 mT) shows regularly spaced CB resonances (see Supplementary Fig. 1a in Supplementary Note 1) for which we find a systematic increase in the total tunnel coupling Γ with increasing V_{BG} (see Supplementary Fig. 1b in Supplementary Note 1), consistent with the lowering of the tunnel barrier when the band structure is shifted to lower energies with respect to the Fermi energy (see schematic in Supplementary Fig. 2 in Supplementary Note 1)[23].

In the device discussed here, the QD is located about $L \approx$ 350 nm from the Al electrode, leaving a bare NW segment of this length between the QD and the SC, which we refer to as the "lead segment" (LS). This provides a new experimental situation, as the QD is not directly coupled to the SC (as it might be the case in other experiments[25–27]) and can be used to probe the LS. V_{BG} here directly tunes the chemical potential in both the LS and the QD. We record G as a function of the bias voltage V_{SD} applied between the SC and the normal metal contact. If the electrons would tunnel directly from the QD to the superconducting electrode, we would expect to see a gap similar to the one of the bulk value $\Delta \approx 210$ μeV[28] of the SC, independent of V_{BG}. As most of the bias drops over the QD, G is proportional to the DOS in the LS. This is the case for positive V_{BG} where carriers accumulate in the NW. Therefore, we can perform spectroscopy on the LS by tunneling from the QD (see Fig. 1b).

An interesting transition in the conductance can already be found in the overview data in Fig. 1c, d presenting regular CB diamonds in the superconducting state (charging energy $E_c \approx 6$ meV, level spacing $\varepsilon \approx 1.5$ meV to 2 meV) for two different regimes of V_{BG}. While for positive gate voltages, $V_{BG} > 3$ V, we observe a superconducting gap around zero bias (c.f. Fig. 1d), for low gate voltages (Fig. 1c) we do not find any features related to superconductivity, but rather the sequence of diamonds expected for the normal state.

The QD can be used as a spectrometer in two different regimes. In the first regime, the QD is kept deep in the CB regime where the charge is fixed for bias voltages in the range of the proximity induced gap Δ^*, as $\Delta^* \ll E_c$. In this regime, transport is mediated by cotunneling, which is a second-order process involving the virtual occupation of a QD state[29]. Here, the QD can be thought of as a single tunnel barrier. In the second regime, the QD electrochemical potential is tuned to a CB resonance, with transport occurring as first order sequential tunneling. In the following, we discuss the experiments in the two regimes one after the other.

Cotunneling spectroscopy. First, we investigate the cotunneling regime, where we can understand the SC–LS as an S-N junction, which is weakly coupled to the QD. An example of a measured spectrum is shown in Supplementary Fig. 3a in Supplementary Note 1. It can be characterized by four quantities: the magnitude of the observed gap Δ^*, the full width at half the maximum (FWHM) of the peaks at the gap edge, the normal state conductance G_N measured at a bias $|V_{SD}| > \Delta^*/e$ and G_S the conductance at $V_{SD} = 0$. As the conductance is not fully suppressed at zero bias, we characterize this softness by defining the suppression factor $S = G_S/G_N$.

Figure 2a–c show G as a function of V_{BG} and V_{SD} for three different backgate regimes. Cross-sections (Fig. 2c: averaged over 20 cross-sections in the CB diamond centers) at different V_{BG} in the CB regime are plotted as blue lines. At large gate voltages ($V_{BG} \approx 7$ V, Fig. 2a) we find a clear gap around zero bias, which

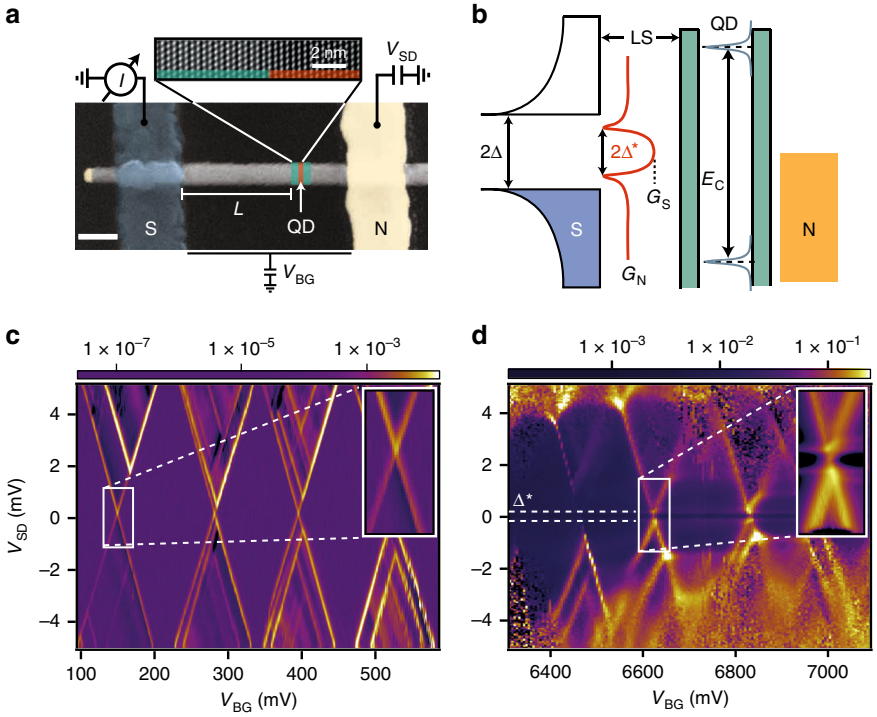

Fig. 1 Crystal phase engineered quantum dot in a superconductor - quantum dot - normal device. **a** False color scanning electron micrograph of the investigated device, consisting of a superconductor S (blue)–indium arsenide (InAs) nanowire (NW)–normal metal N (yellow) junction (scale bar: 100 nm). A quantum dot (QD, red) forms between two in-situ grown tunnel barriers (green) in the wurtzite phase. The distance between the QD and S is $L \approx 350$ nm. The measurement scheme is shown schematically. The inset shows a high-resolution transmission electron micrograph of the atomically sharp zincblende/wurtzite interface of a comparable NW. **b** Schematic energy diagram of such a system with an illustration of the proximity gap Δ^* in the lead segment (LS), with a conductance G_N in the normal and G_S in the superconducting state. **c** Differential conductance G (e^2/h) as a function of the backgate voltage V_{BG} and the source-drain bias V_{SD} in the superconducting state. The inset shows a single Coulomb blockade (CB) resonance in more detail. **d** CB diamonds at V_{BG} exhibiting a gap in the transport characteristics

can be detected down to $V_{BG} \approx 2.6$ V (Fig. 2b). The same cross-sections normalized to G_N are shown in Supplementary Fig. 3a in Supplementary Note 1. All cross-sections exhibit a suppression of G at $V_{SD} = 0$ and $\Delta^* \approx 150$ μeV (position of the peak maxima). The FWHM and S are shown to be roughly constant over the investigated gate range, see Supplementary Fig. 3b in Supplementary Note 1, with FWHM ≈ 65 μeV ± 10 μeV and $S \approx 0.5 \pm 0.1$, respectively. In an ideal SC and weak coupling, S should be close to zero for a strong tunnel barrier. Larger values are often observed for proximity-induced gaps, and referred to as soft-gap[30–32]. For lower gate voltages $V_{BG} < 2.6$ V (Fig. 2b) it is difficult to perform this analysis, because the cotunneling signal is very low compared with the noise floor of the experiment ($G \approx 10^{-5}\, e^2/h$). However, we can still observe broad peaks down to $V_{BG} \approx 1.8$ V. For $V_{BG} < 1.8$ V, the differential conductance is too low to observe any signatures of superconductivity with the resolution of our measurement. For even lower gate voltages $V_{BG} \approx 0.2$ V (Fig. 2c), no features inside the CB diamonds can be resolved anymore. In summary, in the regime accessible by the cotunneling experiments, the proximity gap characteristics are roughly independent of the gate voltage.

Sequential tunneling spectroscopy. To extract characteristics of the LS for a larger gate range than in the cotunneling regime, we now use the QD resonances (first-order process through the QD). Panels (i) ("Exp.") of Fig. 3a–d show detailed measurements of a CB resonance in different backgate regimes, whereas panels (ii) show a simulated map ("model") discussed below, and panels (iii) show cross-sections at V_{BG}, as indicated in panels (i, ii). We will first discuss the experimental results presented in panels (i) of Fig. 3a–d. Afterwards we will compare our findings with the calculated results of a resonant tunneling model, which are presented in panels (ii) of each Fig. 3a–d. In an S–QD–N system, the Coulomb diamond pattern is expected to be affected by superconductivity as presented in Fig. 3e. The tips of the Coulomb diamonds are expected to be shifted by $\Delta V_{SD} = 2\Delta^*/e$ in bias and by $\Delta V_{BG} = 2\Delta^*/\beta e$ in gate voltage (with β the lever arm of the QD)[26,33].

From the QD characteristics in the normal state (see Supplementary Fig. 1a in Supplementary Note 1), we find that the tunnel coupling Γ increases significantly for $V_{BG} > 2.5$ V. For large Γ, e.g., at $V_{BG} \approx 6.6$ V, a CB pattern is shown in Fig. 3a. The CB resonances are broad, but clearly show a suppressed conductance around zero bias. We find a gap of $\Delta^* \approx 150$ μeV, confirming the value obtained in the cotunneling regime (Fig. 2).

A CB resonance with a smaller Γ value at $V_{BG} \approx 2.1$ V is shown in Fig. 3b, which is similar to the one in Fig. 3a, but with an additional resolved resonance. As expected (see Fig. 3e), the "CB diamond tips" are shifted in energy by $\pm\Delta^*/e$ and ΔV_{BG} in gate voltage, yielding a consistent value of $\Delta^* \approx 150$ μeV. We observe an additional resonance that crosses through the gap (white arrows). This line corresponds to the alignment of the Fermi levels of the two reservoirs with the QD state. We attribute this resonance to tunneling through the non-zero DOS remaining at zero bias (see position I in Fig. 3e).

At $V_{BG} \approx 0.2$ V, the conductance suppression is significantly reduced, as shown in Fig. 3c. The CB diamond tips appear to be only slightly separated and shifted. We note that in this gate range we cannot resolve any signal in the cotunneling spectrum, as discussed in Fig. 2.

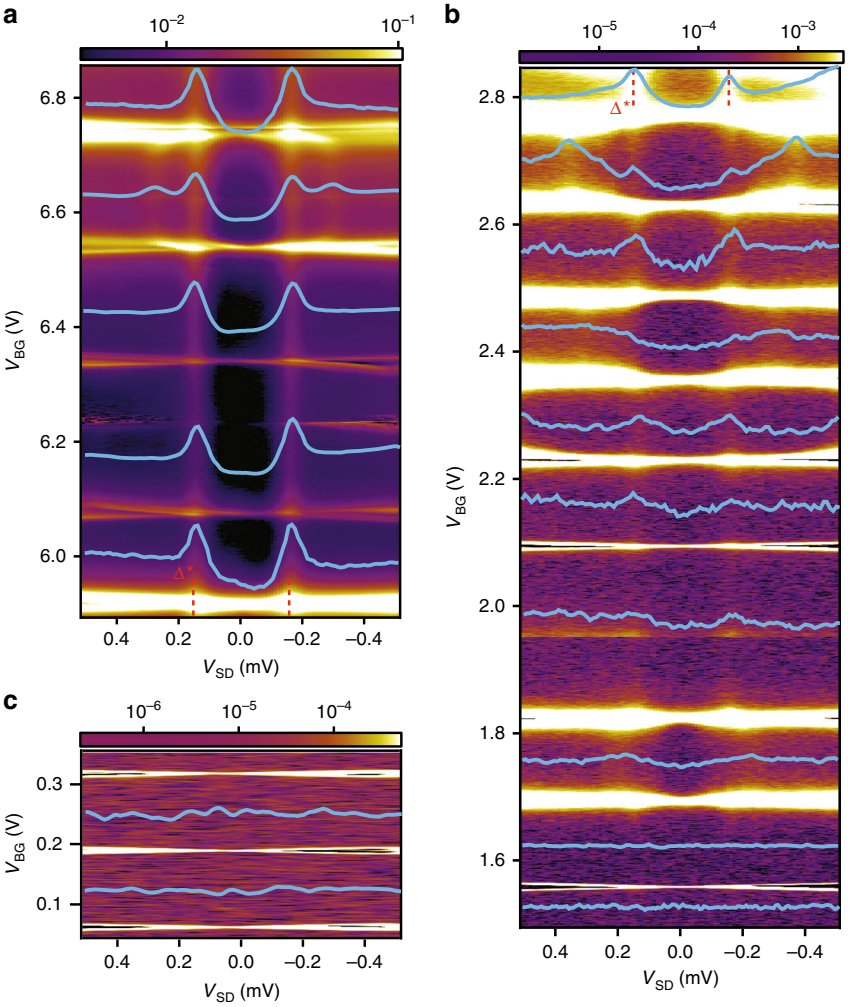

Fig. 2 Proximity gap probed by cotunneling spectroscopy. The color bar is the differential conductance G (e^2/h) as a function of backgate voltage V_{BG} and source-drain voltage bias V_{SD} for **a** high, **b** middle, and **c** low backgate voltages V_{BG}. Blue lines are averaged over 20 cross-sections taken in the center of the Coulomb blockade diamonds. The cross-sections shown in **c** are averaged over the Coulomb blockade region between the Coulomb resonances

At even lower gate voltages, e.g., $V_{BG} \approx 80$ mV (Fig. 3d), we do not observe any influence of the superconducting contact, but a regular CB resonance, as found in the normal state.

To extract the characteristic numbers from these data, we use a resonant tunneling model for a S–QD–N junctions. The current is then given by[26,34] $I = \int_{-\infty}^{\infty} dE D_N(E) \cdot D_S(E + eV_{SD}) \cdot T_{QD}(E, V_{BG}, V_{SD}) \cdot [f_N(E) - f_S(E + eV_{SD})]$, with $D_N(E)$ the constant DOS of the normal metal, $T_{QD}(E, V_{BG}, V_{SD})$ a Lorentzian transmission function, accounting for the resonant tunneling through the QD, and including a broadening due to the finite coupling to the electrodes. $f_{S/N}$ are the Fermi distribution functions for the respective contacts. To account for the softness of the gap, the DOS in the LS can be expressed using the phenomenological Dynes parameter δ by $D_S = |\mathrm{Re}(E - i\delta/\sqrt{(E - i\delta)^2 - \Delta^{*2}})|$[35]. By adjusting the magnitude of the gap Δ^*, the QD resonance broadening Γ and the Dynes parameter δ, we get the conductance maps presented in panel (ii) of each Fig. 3a–d ("model").

We can reproduce the characteristics of the CB resonance in Fig. 3a using $\Gamma = 150$ μeV, which is slightly smaller than what we obtained in the normal state. For the size of the gap we find $\Delta^* = 165$ μeV and $\delta = 0.4 \cdot \Delta^*$ ($\delta = 65$ μeV), resulting in a suppression of $S \approx 0.5$, similar to what is found in the cotunneling regime. To reproduce the data in Fig. 3b, we use $\Gamma = 40$ μeV (similar to the numbers in the normal state), $\Delta^* \approx 145$ μeV and $\delta = 0.4 \cdot \Delta^* (\delta \approx 60$ μeV), i.e., the parameters are almost identical to the ones we obtained in the cotunneling regime at higher gate voltages. The corresponding cross-sections agree well with the experiment. We note that the conductance enhancement at the gap edge, as well as the negative differential conductance are well reproduced by the model. We point out that in the sequential tunneling regime, we can extract gap characteristics down to backgate voltages of 0.2 V, which is not possible in the cotunneling regime.

To reproduce the characteristics of the CB resonance in Fig. 3c ($V_{BG} \approx 200$ mV), we find that the tunnel coupling is similar to the one in Fig. 3b ($\Gamma = 60$ μeV) and $\delta = 0.5 \cdot \Delta^* (\delta \approx 40$ μeV). However, the size of the superconducting energy gap is $\Delta^* \approx 85$ μeV, significantly smaller than that found at larger gate voltages. Also here, the model reproduces the data well, illustrated in the corresponding cross-sections.

Using the resonant tunneling model to simulate the resonance around $V_{BG} \approx 80$ mV (Fig. 3d) we extract $\Gamma = 50$ μeV and an upper limit for Δ^* of 10 μeV. The model reproduces very well the characteristics of the CB resonance, which essentially corresponds to an N–QD–N device. The resonances in the experiment at higher bias outside the CB are due to excited states, which are not included in the model.

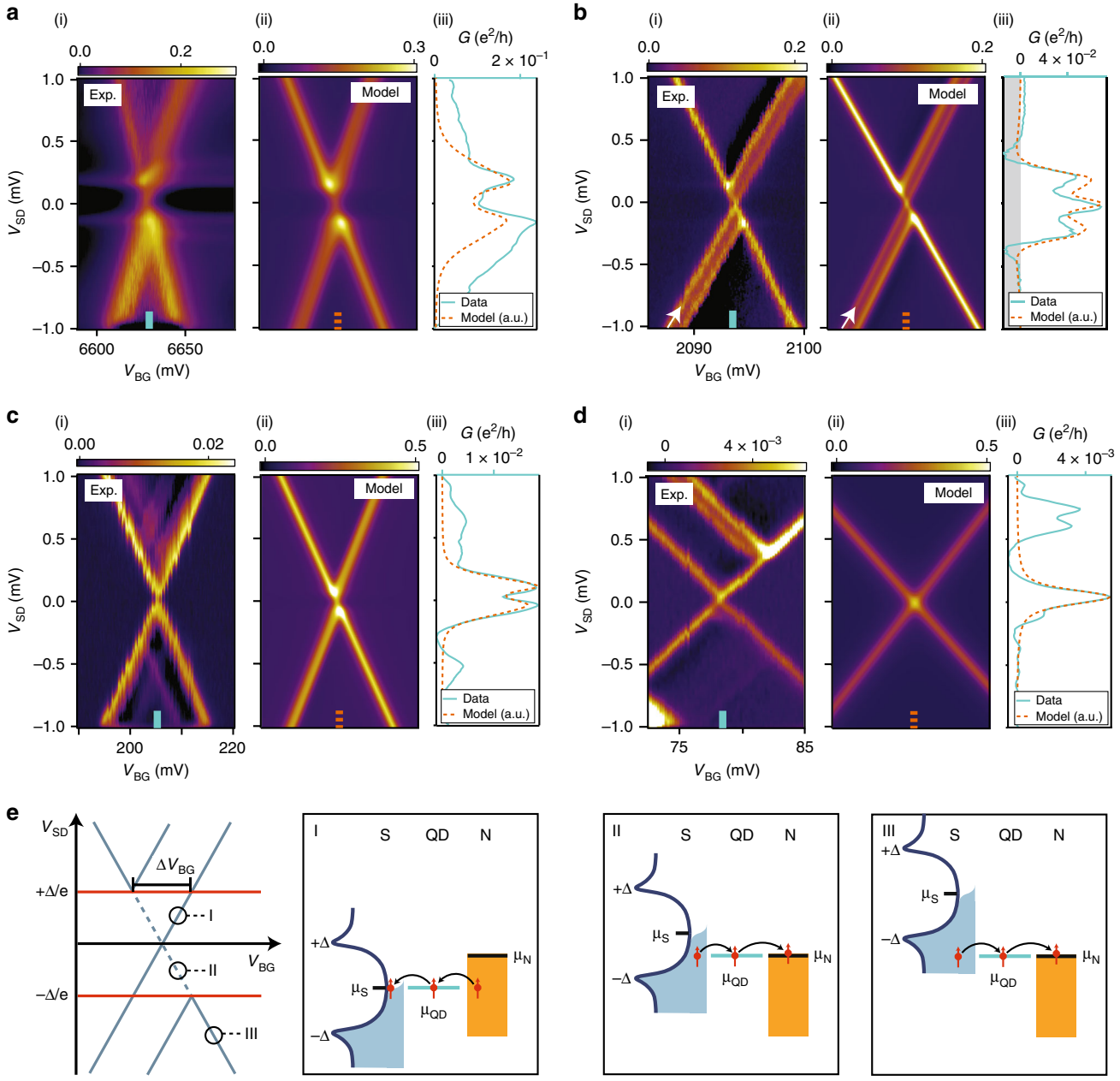

Fig. 3 Proximity gap in the resonant tunneling regime. **a**–**d** Experiment (i), resonant tunneling model (ii), and cross-sections of both (iii) for different Coulomb blockade (CB) resonances. The color bar is the differential conductance G (e^2/h) as a function of the backgate voltage V_{BG} and the source-drain bias voltage V_{SD}. Light green and orange lines indicate the V_{BG} of the cross-sections in (iii). **e** Relative positions of the electrochemical potentials of the normal contact (μ_N), the superconductor ($\mu_S = \mu_N - eV_{SD}$) and the quantum dot (μ_{QD}) for selected points (I, II, III) in the charge stability diagram. The tips of the diamonds are shifted in gate voltage by $\Delta V_{BG} = 2\Delta^*/(\beta e)$ with β the lever arm of V_{BG}. In **a**, the tunnel coupling is almost a factor of 3 larger than in **b**–**d**. From the model, the tunnel coupling Γ is essentially constant for **b**–**d**, whereas the value for the induced superconducting energy gap varies from $\Delta^* =$ 165 μeV in **a**, $\Delta^* = 145$ μeV in **b**, $\Delta^* = 85$ μeV in **c**, to $\Delta^* < 10$ μeV in **d**

To summarize the measurements in the CB resonance regime (Fig. 3), we observe a transition from a region where the LS acts as a superconducting lead (large gate voltages) with $\Delta^* \approx$ 165 μeV to 150 μeV to an intermediate regime with a reduced $\Delta^* \approx 85$ μeV, to a regime without effects of superconductivity. The parameters extracted from the resonant tunneling model demonstrate a clear evolution of Δ^* in the LS.

Discussion

The evolution of the induced gap Δ^* as a function of V_{BG} is summarized in Fig. 4a. The curve shows a sharp transition from a clearly resolved energy gap for $V_{BG} > 0$ to a fully suppressed gap at $V_{BG} < 0$.

Although the observed proximity feature can be well fitted by a broadened BCS DOS, this approach is not an adequate description, as there are only few states in the quasi one-dimensional NW lead. Qualitatively, one can understand the transition by considering only a few modes in the LS. All electrons at energies within the gap of the SC are Andreev reflected (AR) at the SC, giving rise to Andreev-bound states (ABSs).

We interpret the observed transition in Δ^* qualitatively as a gate-tunable transition of ABSs forming in the LS from the long to the short junction limit. Both limits are defined by comparing

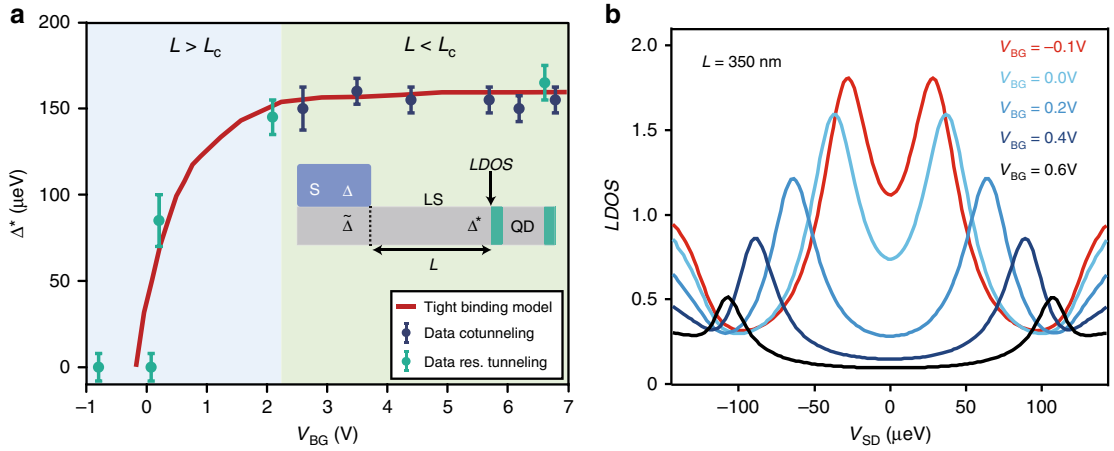

Fig. 4 Proximity induced gap as a function of gate voltage. **a** Proximity gap Δ^* as a function of the backgate voltage V_{BG}. The inset shows a schematic of the device with the relevant parameters: superconducting gap Δ in the bulk superconductor *S*, induced gap $\widetilde{\Delta}$ below the superconductor inside the nanowire (gray), and the induced gap Δ^* in the nanowire lead segment (LS). The quantum dot (QD) is located $L = 350$ nm from *S*. Background colors indicate the short junction limit (green) and the long junction limit (blue), depending on the relation of the the critical length L_c compared with the length of the junction *L*. Bars indicate the uncertainty of the extracted values of Δ^*. **b** Calculated local density of states (LDOS) as a function of energy for different gate voltages V_{BG} at a fixed distance from the interface, $L = 350$ nm

the physical length of the junction, *L*, with the characteristic length scale $L_c = \hbar v_F/\widetilde{\Delta}$, which is often called coherence length in the ballistic limit[36]. Assuming a rather low Fermi velocity ($v_F = 2 \times 10^5$ m/s), we find $L_c \approx 850$ nm. Here v_F is the Fermi velocity in the LS, $\hbar$ the Planck constant, and $\widetilde{\Delta}$ the proximity gap induced by the aluminum contact in the NW directly below the SC (see inset of Fig. 4a).

In the short junction limit ($L \ll L_c$) the energy of the ABSs (E_{ABS}) in the LS is dominated by the phase change due to AR at the SC/LS interface (dashed line in schematic), where $\widetilde{\Delta}$ is assumed to change abruptly. In this limit, the energies of the ABSs are "pushed" to $E_{ABS} \cong \widetilde{\Delta}$, resulting in a superconducting proximity gap in the LS similar to $\widetilde{\Delta}$, i.e., $\Delta^* \sim \widetilde{\Delta}$[37]. In the long junction limit ($L \gg L_c$), E_{ABS} is determined by the phase acquired in the LS, which scales with $k_F = m^* \cdot v_F/\hbar \propto v_F$, with m^* the effective electron mass. In this limit, E_{ABS} can take on smaller values, thus filling the proximity gap[36]. We therefore can tune E_{ABS} by tuning v_F and the electron density in the LS using V_{BG}. For very positive gate voltages, E_F is relatively far up in the conduction band with a correspondingly large v_F, resulting in a large L_c, bringing the LS to the short junction limit, $L < L_c$. In contrast, when we align the bottom of the conduction band to E_F by lowering V_{BG}, v_F and L_c are strongly reduced, bringing the LS into the long junction limit, $L > L_c$, and $E_{ABS} < \widetilde{\Delta}$. As a result, the apparent gap Δ^* is reduced by the ABSs moving into the gap. We note that $\widetilde{\Delta}$ in the NW segment below the SC is screened by the SC and is therefore not gate tunable.

To support this qualitative picture, we employ a numerical model, in which we combine the Green's function method with a tight binding model. The properties of the SC are taken into account as a self-energy dressing the bare Green's function in a NW section below *S*, where a superconducting gap $\widetilde{\Delta}$ is induced depending only on the coupling to *S* (details can be found in the Supplementary Note 2). This region is coupled to a bare NW segment (of length $L = 350$ nm) modeling the LS (see inset of Fig. 4a). We then investigate the local DOS at a distance $L = 350$ nm as a function of the gate voltage in the NW (Fig. 4b). Like for the experimental data, we extract Δ^* as the distance between the maxima in the DOS. Here the number of ABSs as well as the ABS energy is determined by the length of the LS. The resulting Δ^* of this calculation is plotted as a function of V_{BG} as a red line in Fig. 4a.

In excellent agreement with the experiment, we observe a sharp transition in the detected gap, corresponding to the transition from the short to the long junction limit. In the model, Δ^* tends to zero when E_F is aligned to the bottom of the conduction band ($V_{BG} \approx -0.2$ V), just before the LS is fully depleted and $v_F \to 0$. For a better understanding we study the dependence of an individual ABS as a function of V_{BG} in Supplementary Fig. 4 in the Supplementary Note 3. Evolving from the long to the short junction limit, the states with energy $E < \Delta^*$ move toward the gap, resulting in a fully formed smooth proximity gap Δ^*. We note that in this model the width of the ABS is a free parameter, which we set to 25 μeV. In seeming contradiction to the depleted LS, the experiment still shows several CB resonances below this gate voltage, which we attribute to evanescent modes from the NW segment below *S* (which is not depleted) that couples weakly to the QD wavefunctions, rendering the QD couplings highly asymmetric with very low transmission amplitudes, as observed in the experiment.

The gap in our devices is soft, i.e., the conductance suppression at zero bias is significantly lower than in NWs with an epitaxial Al shell[38,39]. The reason for this remains unclear and is a priori not expected from the model. The evaporated bulk Al shows a hard gap ($S \approx 0.01$) when used in standard, large-area metallic S–I–S tunnel junctions measured in a similar experimental setup (see Supplementary Fig. 5 in Supplementary Note 4). Introducing random spatial potential fluctuations at the NW–S interface[40,41] in the presented numerical model does not account for the observed small suppression either (see Supplementary Fig. 6 in Supplementary Note 5). However, we cannot exclude other types of disorder or non-ideal material interfaces as the origin of the "soft gap". In the ABS picture, the softness of the gap is determined by the life time of the ABSs in the LS. This broadening can have different physical origins, namely (1) tunneling to the QD, which should exhibit a similar tunability as the QD life time, (2) single particle tunneling to the NW segment below *S*, e.g., by an inverse proximity effect due to the gold nanoparticle used for the NW growth, and (3) quasiparticle excitation by microwave radiation absorption that might be different in NW devices compared to metallic ones.

In conclusion, we present a systematic study of the apparent transport gap in a NW segment induced by a proximity coupled

SC. For this purpose we introduce QD tunnel spectroscopy enabled by in-situ-grown axial tunnel barriers. We observe a gate-tunable transition of the gap amplitude from a fully developed, constant proximity gap at large electron densities to smaller values and ultimately a complete suppression of the gap at low densities. The data are consistent with a transition from the short junction limit of an S-N device to the long junction limit with ABSs forming at energies also below the gap energy. This transition occurs when the Fermi energy is close to the bottom of the conduction band and the respective Fermi velocity tends toward zero. Our experiments demonstrate that NWs with in-situ-grown barriers, in our example with crystal phase engineered barriers, are very useful to perform transport spectroscopy in SC–semiconductor hybrid systems. We have thus introduced a novel spectroscopy tool, which is well suited to study superconducting bound states in semiconducting NWs, and might be useful to tackle fundamental limitations found in recent studies of Majorana-bound states[42,43]. The next steps toward investigating Majorana devices on this platform include technological progress, e.g., the possibility to contact the NW epitaxially with a SC as well as precise alignment of this contact close to the in-situ-grown QD.

Methods

Fabrication and measurement techniques. The InAs NWs were grown by metal-organic-vapor-phase epitaxy and have an average diameter of 70 nm. The two segments of WZ crystal phase forming the tunnel barriers have a thickness of 30 nm. The zinc-blende segment in between, which defines the QD, has a width of 25 nm.

The NWs were transferred mechanically from the growth substrate to a degenerately *p*-doped silicon substrate with a SiO_2 capping layer (400 nm). The substrate is used as a global back gate. For the electron beam lithography we employ pre-defined markers and contact pads made of Ti/Au (5 nm /45 nm). The normal metal contact to the NW is made of Ti/Au (5 nm/70 nm) and the superconducting contact of Ti/Al (5 nm/80 nm). Before each evaporation step, the native oxide of the NW is removed by an Argon ion sputtering.

All measurements were carried out in a dilution refrigerator at a base temperature of 20 mK. Differential conductance has been measured using standard lock-in techniques ($V_{ac} = 10\,\mu V$, $f_{ac} = 278$ Hz).

Data availability

The datasets generated during and/or analyzed during the current study are available from the corresponding author on reasonable request.

Received: 6 January 2019 Accepted: 13 May 2019
Published online: 03 July 2019

References

1. Beenakker, C. W. J. Quantum transport in semiconductor-superconductor microjunctions. *Phys. Rev. B* **46**, 12841–12844 (1992).
2. Hofstetter, L., Csonka, S., Nygård, J. & Schönenberger, C. Cooper pair splitter realized in a two-quantum-dot y-junction. *Nature* **461**, 960–963 (2009).
3. Schindele, J., Baumgartner, A. & Schönenberger, C. Near-unity cooper pair splitting efficiency. *Phys. Rev. Lett.* **109**, 157002 (2012).
4. Cleuziou, J.-P., Wernsdorfer, W., Bouchiat, V., Ondarçuhu, T. & Monthioux, M. Carbon nanotube superconducting quantum interference device. *Nat. Nanotechnol.* **1**, 53–59 (2006).
5. Mourik, V. et al. Signatures of majorana fermions in hybrid superconductor-semiconductor nanowire devices. *Science* **336**, 1003–1007 (2012).
6. Albrecht, S. M. et al. Exponential protection of zero modes in majorana islands. *Nature* **531**, 206–209 (2016).
7. Deng, M. T. et al. Majorana bound state in a coupled quantum-dot hybrid-nanowire system. *Science* **354**, 1557–1562 (2016).
8. Zhang, H. et al. Quantized majorana conductance. *Nature* **556**, 74–79 (2018).
9. Alicea, J., Oreg, Y., Refael, G., von Oppen, F. & Fisher, M. P. A. Non-abelian statistics and topological quantum information processing in 1d wire networks. *Nat. Phys.* **7**, 412–417 (2011).
10. Nayak, C., Simon, S. H., Stern, A., Freedman, M. & Sarma, S. D. Non-abelian anyons and topological quantum computation. *Rev. Mod. Phys.* **80**, 1083–1159 (2008).
11. Leijnse, M. & Flensberg, K. Scheme to measure majorana fermion lifetimes using a quantum dot. *Phys. Rev. B* **84**, 140501 (2011).
12. Hoffman, S., Chevallier, D., Loss, D. & Klinovaja, J. Spin-dependent coupling between quantum dots and topological quantum wires. *Phys. Rev. B* **96**, 045440 (2017).
13. Chevallier, D., Szumniak, P., Hoffman, S., Loss, D. & Klinovaja, J. Topological phase detection in rashba nanowires with a quantum dot. *Phys. Rev. B* **97**, 045404 (2018).
14. Gharavi, K., Hoving, D. & Baugh, J. Readout of majorana parity states using a quantum dot. *Phys. Rev. B* **94**, 155417 (2016).
15. van Dam, J. A., Nazarov, Y. V., Bakkers, E. P. A. M., Franceschi, S. D. & Kouwenhoven, L. P. Supercurrent reversal in quantum dots. *Nature* **442**, 667–670 (2006).
16. Lee, E. J. H. et al. Spin-resolved andreev levels and parity crossings in hybrid superconductor–semiconductor nanostructures. *Nat. Nanotechnol.* **9**, 79–84 (2013).
17. Guéron, S., Pothier, H., Birge, N. O., Esteve, D. & Devoret, M. H. Superconducting proximity effect probed on a mesoscopic length scale. *Phys. Rev. Lett.* **77**, 3025–3028 (1996).
18. Cherkez, V. et al. Proximity effect between two superconductors spatially resolved by scanning tunneling spectroscopy. *Phys. Rev. X* **4**, 011033 (2014).
19. Dick, K. A., Thelander, C., Samuelson, L. & Caroff, P. Crystal phase engineering in single InAs nanowires. *Nano Lett.* **10**, 3494–3499 (2010).
20. Lehmann, S., Wallentin, J., Jacobsson, D., Deppert, K. & Dick, K. A. A general approach for sharp crystal phase switching in InAs, GaAs, InP, and GaP nanowires using only group v flow. *Nano Lett.* **13**, 4099–4105 (2013).
21. Rossella, F. et al. Nanoscale spin rectifiers controlled by the stark effect. *Nat. Nanotechnol.* **9**, 997–1001 (2014).
22. Nilsson, M. et al. Tuning the two-electron hybridization and spin states in parallel-coupled InAs quantum dots. *Phys. Rev. Lett.* **121**, 156802 (2018).
23. Nilsson, M. et al. Single-electron transport in InAs nanowire quantum dots formed by crystal phase engineering. *Phys. Rev. B* **93**, 195422 (2016).
24. Chen, I.-J. et al. Conduction band offset and polarization effects in InAs nanowire polytype junctions. *Nano Lett.* **17**, 902–908 (2017).
25. Doh, Y.-J., Franceschi, S. D., Bakkers, E. P. A. M. & Kouwenhoven, L. P. Andreev reflection versus coulomb blockade in hybrid semiconductor nanowire devices. *Nano Lett.* **8**, 4098–4102 (2008).
26. Gramich, J., Baumgartner, A. & Schönenberger, C. Resonant and inelastic andreev tunneling observed on a carbon nanotube quantum dot. *Phys. Rev. Lett.* **115**, 216801 (2015).
27. Gramich, J., Baumgartner, A. & Schönenberger, C. Andreev bound states probed in three-terminal quantum dots. *Phys. Rev. B* **96**, 195418 (2017).
28. Court, N. A., Ferguson, A. J. & Clark, R. G. Energy gap measurement of nanostructured aluminium thin films for single cooper-pair devices. *Supercond. Sci. Technol.* **21**, 015013 (2007).
29. Franceschi, S. D. et al. Electron cotunneling in a semiconductor quantum dot. *Phys. Rev. Lett.* **86**, 878–881 (2001).
30. Doh, Y.-J. Tunable supercurrent through semiconductor nanowires. *Science* **309**, 272–275 (2005).
31. Sand-Jespersen, T. et al. Kondo-enhanced andreev tunneling in InAs nanowire quantum dots. *Phys. Rev. Lett.* **99**, 126603 (2007).
32. Jellinggaard, A., Grove-Rasmussen, K., Madsen, M. H. & Nygård, J. Tuning Yu-Shiba-Rusinov states in a quantum dot. *Phys. Rev. B* **94**, 064520 (2016).
33. Gramich, J., Baumgartner, A. & Schönenberger, C. Subgap resonant quasiparticle transport in normal-superconductor quantum dot devices. *Appl. Phys. Lett.* **108**, 172604 (2016).
34. Yeyati, A. L., Cuevas, J. C., López-Dávalos, A. & Martn-Rodero, A. Resonant tunneling through a small quantum dot coupled to superconducting leads. *Phys. Rev. B* **55**, R6137–R6140 (1997).
35. Dynes, R. C., Narayanamurti, V. & Garno, J. P. Direct measurement of quasiparticle-lifetime broadening in a strong-coupled superconductor. *Phys. Rev. Lett.* **41**, 1509–1512 (1978).
36. Bagwell, P. F. Suppression of the josephson current through a narrow, mesoscopic, semiconductor channel by a single impurity. *Phys. Rev. B* **46**, 12573–12586 (1992).
37. Bena, C. Metamorphosis and taxonomy of andreev bound states. *Eur. Phys. J. B* **85**, 196 (2012).
38. Krogstrup, P. et al. Epitaxy of semiconductor–superconductor nanowires. *Nat. Mater.* **14**, 400–406 (2015).
39. Chang, W. et al. Hard gap in epitaxial semiconductor–superconductor nanowires. *Nat. Nanotechnol.* **10**, 232–236 (2015).
40. Takei, S., Fregoso, B. M., Hui, H.-Y., Lobos, A. M. & Sarma, S. D. Soft superconducting gap in semiconductor majorana nanowires. *Phys. Rev. Lett.* **110**, 186803 (2013).
41. Liu, C.-X., Setiawan, F., Sau, J. D. & Sarma, S. D. Phenomenology of the soft gap, zero-bias peak, and zero-mode splitting in ideal majorana nanowires. *Phys. Rev. B* **96**, 054520 (2017).

42. Liu, C.-X., Sau, J. D., Stanescu, T. D. & Sarma, S. D. Andreev bound states versus majorana bound states in quantum dot-nanowire-superconductor hybrid structures: Trivial versus topological zero-bias conductance peaks. *Phys. Rev. B* **96**, 075161 (2017).
43. Reeg, C., Dmytruk, O., Chevallier, D., Loss, D. & Klinovaja, J. Zero-energy andreev bound states from quantum dots in proximitized rashba nanowires. *Phys. Rev. B* **98**, 245407 (2018).

Acknowledgements

This work has received funding from the Swiss National Science Foundation, the Swiss Nanoscience Institute, and the Swiss NCCR QSIT. C.S. has received funding from the European Research Council (ERC) under the European Unions Horizon 2020 research and innovation program: grant agreement 787414, ERC-Adv TopSupra. D.C. received funding from the European Unions Horizon 2020 research and innovation program (ERC Starting Grant, agreement number 757725). S.L., M.N., K.A.D. and C.T. acknowledge financial support by the Knut and Alice Wallenberg Foundation (KAW) and the Swedish Research Council (VR). We thank C. Reeg and S. Hoffman for fruitful discussions.

Author contributions

C.J. fabricated the devices and performed the measurements together with R.D. C.J., R.D. and A.B. analyzed the data. A.B. provided the resonant tunneling model. D.C. provided the numerical calculations. S.L., M.N., K.A.D. and C.T. developed the nanowire structure. C.S. and A.B. planned and designed the experiments, and participated in all discussions. All authors contributed to the manuscript.

Additional information

Supplementary information accompanies this paper at https://doi.org/10.1038/s42005-019-0162-4.

Competing interests: The authors declare no competing interests.

Reprints and permission information is available online at http://npg.nature.com/reprintsandpermissions/

Publisher's note: Springer Nature remains neutral with regard to jurisdictional claims in published maps and institutional affiliations.